

A bioactivated in vivo assembly (BIVA) nanotechnology fabricated NIR probe for small pancreatic tumor intraoperative navigation imaging

Li-Li Li (✉ lill@nanoctr.cn)

CAS Center for Excellence in Nanoscience, CAS Key Laboratory for Biomedical Effects of Nanomaterials and Nanosafety, National Center for Nanoscience and Technology (NCNST) <https://orcid.org/0000-0002-9793-3995>

Han Ren

National Center for Nanoscience and Technology (NCNST)

Xiao-Xiao Zhao

National Center for Nanoscience and Technology (NCNST)

Dayong Hou

the Fourth Hospital of Harbin Medical University

Haodong Yao

Institute of High Energy Physics <https://orcid.org/0000-0001-5959-8594>

Lina Zhao

Institute of High Energy Physics, Chinese Acad Sci <https://orcid.org/0000-0002-9796-0221>

Wanhai Xu

Fourth Affiliated Hospital of Harbin Medical University

Hao Wang

National Center for Nanoscience and Technology

Article

Keywords: bioactivated in vivo assembly (BIVA), visual intraoperative navigation, bioactivated in vivo assembly (BIVA) nanotechnology,

Posted Date: April 30th, 2021

DOI: <https://doi.org/10.21203/rs.3.rs-445085/v1>

License:   This work is licensed under a Creative Commons Attribution 4.0 International License.
[Read Full License](#)

Version of Record: A version of this preprint was published at Nature Communications on January 20th, 2022. See the published version at <https://doi.org/10.1038/s41467-021-27932-y>.

Abstract

Visual intraoperative navigation depends on the optical technique for real-time imaging of the boundary of tumor. However, the fluorescence probes now enable for bioimaging are usually lack of tumor specificity and poor imaging window, which limited the further clinical applications. Here, we report a bioactivated in vivo assembly (BIVA) nanotechnology, which provides a universal optical probe delivery system to enhance the targeting specificity, region accumulation and continuous imaging window of the probe. Based on the coupling of BIVA domain and probe, BIVA probe exhibits a synergy mechanism of active targeting and assembly induced retention, which improved the targeting efficiency. In addition, the tumor surface specific nanofiber assembly significantly increases the accumulation of the probe at tumor boundary. The PEGylation of the BIVA probe extended the blood circulation time for 110 min, and the area under the curve (AUC 0-120 h) of tumor was significantly increased by 3.6 times compared with the active targeting probe. As the dynamic assembly difference between tumor and background further enlarges the metabolic difference, we obtained a delayed imaging window between 8-96 hours with better signal-to-background ratio (SBR > 9 times). Our BIVA probe can be used for imaging of small-size ($d < 2$ mm) orthotopic pancreatic tumors in vivo. The high specificity and sensitivity of the BIVA probe will further benefit the intraoperative navigation imaging in clinical.

Introduction

Surgical resection remains the mainstay of treatment for patients with tumor of any grade, including pancreatic cancer, which known as the "king of cancer".^[1-2] However, for small lesions or small metastases in pancreatic cancer (tumor diameter < 2.0 cm), which could be hardly identified currently, are truly dependent on the experience and expertise of the

surgeon.^[3] Otherwise, according to the diagnosis of the cutting edge which is made by intraoperative frozen pathological section, the accuracy rate is only about 50%, which greatly increased the risk of recurrence and metastasis.^[4] It can be found that the 5-year survival rate of pancreatic cancer without metastasis and whose tumor diameter less than 2.0 cm can be increase to 19-41% after surgical resection.^[5] Meantime, the risk of perioperative morbidity can be minimized through the combined use of MIR/CT imaging before operation and fluorescence-based intraoperation imaging.^[6-8]

As a real-time tumor imaging molecule, fluorescent probe has been widely used in clinical practice to provide information on tumor diagnosis and drug development.^[9-12] The most famous probe is indocyanine green (ICG), which is a Food and Drug Administration (FDA)-approved near-infrared fluorescent dye, has been used in clinical intraoperation navigation.^[13] These small molecules lack of active targeting and have a poor retention in tumor, which narrowed the detection window for complicated surgery.^[11] For a better specificity, researchers developed tumor microenvironment turn-on probe to response ROS, lack of oxygen, pH etc.^[14-16] However, traditional small molecule fluorescent dyes metabolize quickly and are easy to be removed by liver and kidney, which shortens the imaging detection

time.^[17] Secondly, the aggregation-caused quenching (ACQ) effect of such fluorescence dyes limited the molecule accumulation in tumor and the photobleaching behavior also confused the imaging. Other way in recent years, the delivery of fluorescent probes *in vivo* has attracted much attention.^[18] Like drug delivery,^[19] fluorescent probes need to be transmitted through blood to the tumor site for better osmotic enrichment at the tumor site to generate fluorescence in a stable and long-term manner.^[20-21]

Herein, we reported a bioactivated *in vivo* assembly (BIVA) probe (named **M1**) for specific and sensitive pancreatic tumor imaging (Fig.1). The BIVA probe was modular designed with five modules, including long-term circulation motif (mPEG₂₀₀₀), response tailoring motif (Gly-Pro-Ala), self-assembly motif (Lys-Leu-Val-Phe-Phe-Gly-Cys-Gly), targeting motif (Arg-Gly-Asp) and imaging motif (IR₇₈₃). Firstly, the probe enabled to long-term blood circulate and had more probability to reach to its target. Next, the targeting motif (RGD) specific recognized and bonded onto the receptor $\alpha v \beta 3$ integrin. The over expressed fibroblast activation protein- α (FAP- α) on the membrane of cancer-associated fibroblasts (CAFs) tailored the molecules to induce *in situ* assembly with typical β -sheet structure. Finally, the assembled nanofibers located around the membrane of CAFs in the tumor microenvironment and well labeled the edge of tumor. Based on *in vivo* self-assembly nanotechnology, the BIVA probe endowed an optimized biodistribution half-life (long blood circulation) and elimination half-life (assembled induced retention effect) with dramatically enhanced area under the curve (AUC) leading to increased drug availability. Otherwise, the targeting and tailoring induced assembly on the membrane of CAFs had a spatial controlled specificity, which also contributed to enhance tumor imaging sensitivity. In this work, we provided an optimized imaging probe delivery system based on BIVA effect, which exhibited a synergetic and enhanced new targeting mechanism: active targeting plus assembly induced retention (AIR) effect. We believed that such a BIVA effect and modular designed BIVA probe will offer us a tool for different imaging molecule delivery.

Results And Discussion

Molecular design, assembled behavior and conformation. In order to study the molecular design and their assembly behavior, we modular designed and synthesized seven molecules (Table 1), which respectively were BIVA probe: **M1** (mPEG-GPAKLVFFGC(IR783)GRGD); the non- FAP- α tailoring molecule: **M2** (mPEG-GPAKLVFFGC(IR783)GRGD) scrambled response tailoring motif of Gly-Pro-Ala with Ala-Gly-Gly; the non-labeling molecule of **M1**: **M3** (mPEG-GPAKLVFFGCGRGD) removed IR₇₈₃ labeling; FAP- α tailoring residue of **M1**: **R-M1** (AKLVFFGC(IR783)GRGD); the non-targeting molecule: **M4** (mPEG-GPAKLVFFGC(IR783)GDTG) scrambled targeting tailoring motif of Arg-Gly-Asp with Asp-Thr-Gly; the non-labeling molecule of **M2**: **M5** (mPEG-AGGKLVFFGCGRGD) removed IR₇₈₃ labeling; FAP- α tailoring residue of **M3**: **R-M3** (AKLVFFGCGRGD). All the synthesized procedure (Supplementary Fig. S1) and the characterizations of these seven molecules can be found in SI (Supplementary Fig. S2-Fig. S8). As seen in Table 1, although scrambled the tailoring motif of **M2** and targeting motif of **M4**, the critical assembly concentration (CAC) of these two molecules in aqueous solution was like that of **M1**, both of which were above 500 μ M. In the absence of IR₇₈₃ labeling, the CAC values of **M3** and **M5** molecules in solution were lower than that of **M1** and **M2**, which was due to that fact that the steric hindrance of hydrophilic IR₇₈₃

was closed to the self-assembly motif (Supplementary Fig. S9). When we removed the long-term circulation motif of mPEG₂₀₀₀ tail of **M1** and **M3**, the CAC of the truncated residues of **R-M1** and **R-M3** dramatically decreased by more than two orders of magnitude (Supplementary Fig. S10). The CAC was quantitatively calculated by β -sheet structure sensitive fluorescence probe Thioflavin T (ThT). All the results indicated that both hydrophilic mPEG tail and IR₇₈₃ labeling contributed to the solubility of molecules in aqueous solution.

Table 1. The sequence, assembled behavior, targeting and tailoring capability of different designed molecules.

Name	Molecular sequence ^a	Critical assembly concentration (CAC) ^b (μ M)	Targeting receptor	Tailoring enzyme
M1	mPEG-GPAKLVFFGC(IR ₇₈₃)GRGD	>500	α v β 3	FAP- α
M2	mPEG-AGGKLVFFGC(IR ₇₈₃)GRGD	>500	α v β 3	-
M3	mPEG-GPAKLVFFGCGRGD	>303.7	α v β 3	FAP- α
R-M1	AKLVFFGC(IR ₇₈₃)GRGD	37.2	α v β 3	-
M4	mPEG-GPAKLVFFGC(IR ₇₈₃)GDTG	>500	-	FAP- α
M5	mPEG-AGGKLVFFGCGRGD	>332.7	α v β 3	-
R-M3	AKLVFFGCGRGD	19.2	α v β 3	-

^a mPEG was methoxy polyethylene glycol with a molecular weight around 2000.

^b the CAC was carried out based on the Thioflavin T (ThT) analysis.

Through the molecular dynamics (MD) simulation calculations,^[22] it was clearly observed that both the backbones of **M1** and the residual **R-M1** of **M1** were β -hairpin conformations (Fig. 2). The mPEG tail was close to the self-assembly motif through multiple hydrophobic interactions to stabilize its conformation, including hydrogen bonds VAL4:CYS8, ARG10:ALA1, ARG10: Cy, ARG10:CASP12, ARG10:CASP12, and salt-bridge ARG10:CASP12 on the both side of the hairpin. Interestingly, the labeling of IR₇₈₃ was almost perpendicular to the β -hairpin backbone and mPEG tail, which formed a significant steric hindrance preventing the further intermolecular assembly. When the mPEG motif was tailored, the backbone of **R-M1** remained its β -hairpin structures by hydrophobic interactions, hydrogen bonds GLY9:PHE6, LYS2:CASP12, ARG10:CASP12, LYS2:CASP12, ARG10:CASP12 and salt-bridges LYS2:CASP12, ARG10:CASP12 on the both side of the hairpin, while the IR₇₈₃ showed an obvious intramolecular rearrangement, resulting in its alignment parallel to the backbone. The decrease of hydrophilicity of molecule and the exposure of hydrogen bonds on the self-assembled surface were beneficial to the occurrence of intermolecular dynamic assembly.

To further evaluate the assembled structures, the corresponding Circular Dichroism (CD), Fourier Transform Infrared (FTIR) and Wide Angle X-ray Scattering (WAXS) spectra were characterized. As shown in Fig. 3a, CD spectrum of **M3** assemblies had a positive band at $\lambda=193$ nm and two negative bands at

$\lambda=208$ nm, $\lambda=225$ nm respectively, which implied a β -sheet and α -helix hybrid structure. In contrast, under the same concentration, **M1** molecules had a random coil secondary structure in CD spectrum as monomers. Meantime, the FTIR spectra of **M1** and **M3** in Fig. 3b clearly observed the intermolecular interactions. The typical fingerprint peaks of β -sheet fibril structure in the amide I region (1700 - 1620 cm^{-1}) included 1694 cm^{-1} , 1662 cm^{-1} and 1631 cm^{-1} .^[23] Whereas, the broad peak at 1647 cm^{-1} indicated that the structure of **M1** was disordered. The above evidences indicated that the **M3** molecule was easier to assemble than **M1** in the absence of IR₇₈₃, and the driving forces of assembly depends on the multiple hydrogen bonds and other weak interactions of the self-assembly motif. After tailoring the hydrophilic balance of mPEG, the **R-M1** exhibited a well-ordered β -sheet assembled secondary structures with a typical strong positive band at 196 nm and a wide negative band at 216 nm (Fig. 3c).

The **R-M1** molecules had a rapid dynamic assembly process within minutes, and the assemblies in aqueous solution had obvious Dunder phenomenon. As a homologous sequence with amyloid β -protein ($A\beta$), the self-assembly motif of peptide sequence of KLVFFGCG was similar to that of ($A\beta$)₄₂ peptide in aggregation kinetics, i.e. dynamic growth from oligomers to amyloid fibrils.^[24] The aggregation starting from the freshly isolated monomers of **R-M1**, the precipitates were separated in 1 minute and 1 hour, respectively. The FTIR spectra of these two samples (Fig. 3d) exhibited completely different spectral features. The rapid separated one had a broad peak at 1634 cm^{-1} , which was identified as oligomer; while the one with extended aggregated time had three weak peaks at 1696 cm^{-1} , 1673 cm^{-1} and 1633 cm^{-1} respectively, which indicating as anti-parallel β -sheet fibrils.^[25-26] Characteristic of nucleated growth procedure (Fig. 3e), the aggregation curves with ThT trace had a growth phase for primary process from the initial 17 min, an elongation phase for surface-catalyzed secondary process between 17-30 min, and a final plain phase after 30 min. The dynamic growth procedure was like the 8-anilino-1-naphthalenesulfonic acid (ANS) stained curve (Supplementary Fig. S11). As known, ANS was sensitive to hydrophobic interaction.^[27] When **R-M1** were in the initial oligomer, the fluorescence intensity of ANS increased due to the enhanced hydrophobicity. When the molecules were elongated and stacked in a higher ordered nanofibrils, the blue shift of ANS in the β -sheet structures reduced the fluorescence. The molecular packing mode of well-ordered fibrils of **R-M1** in Fig. 3f observed a weak reflection at 4.9 Å as laminates space and a strong broad reflection at 10.3 Å as sheet space, which was illustrated in the inserted figure. The fibril morphology was characterized by Transmission Electron Microscope (TEM) imaging (Fig. 3g). The statistical calculation of the fiber diameter in TEM images was 5.0 ± 0.4 nm (Supplementary Fig. S12), which was well corresponding to the theoretical calculated two molecule length of **R-M1**. We assumed that the nanofibers were assembled by twisted **R-M1** molecules centered on self-assembly motif.

Specific enzyme tailoring induced nanofibril assembly. To further investigate the FAP- α specific tailoring and BIVA probe assembly *in situ* simultaneously (Fig. 4a), the High-Performance Liquid Chromatography (HPLC), TEM and Matrix-Assisted Laser Desorption/Ionization Time-of-Flight (MALDI-TOF) mass spectrometry were all used for characterizations. To specifically cleave the response tailoring motif (Gly-Pro-Ala), the pre-synthesized molecules **R-M3**, **M3** and **M5** were set as controls. After incubation with FAP-

α for 12 h, the **M3** molecules were totally cleaved by the enzyme (Fig. 4b), resulting in truncated residues with different retention times compared to **M3** (29.5 min). Compared the residues peaks with **R-M3**, the primary sharp peak at 27.4 min can be identified by the **R-M3** control (27.6 min). Meantime, the wide peak at 14.6 min might be the rest PEG residue. In a sharp contrast, after incubation FAP- α with **M5**, there was no change of the retention peak, which double conformed that the GPA was the FAP- α specific recognized sequence and the molecule was cut between the amino acid of Pro and Ala. After hydrolyzed by FAP- α , the residues of **M1** *in situ* assembled into nanofibers structures under the complex buffer (Fig. 4c and Supplementary Fig. S13). The tailored residues were identified by MALDI-TOF (Fig. 4d), which revealed that **M1** were cut into two parts of **R-M1** and PEG residue. Additionally, when the molecules of **M1** were incubated with Miapaca-2 cells for 2 h, the cell lysis was observed to split into layers. MALDI-TOF confirmed that **R-M1** in the precipitate might be the assembly induced precipitate, and the supernatant obviously contained the PEG residues (Supplementary Fig. S14). In order to further evaluate the specificity of **M1** for different enzymes, including FAP- α , pepsin, pancreatin, lipase and BSA, we used ThT (Thioflavin T) as a detection probe (Fig. 4e). After co-incubation with **M1** for 12 h, only FAP- α group strikingly enhanced the fluorescence intensity, which indicated that **M1** molecule had specificity for FAP- α induced *in situ* assembly.

Enhanced targeting and in situ high efficiency nanofiber formation located cell outline. In design, the bioactivated in vivo assembly (BIVA) was a triggered and synchronous dynamic assembly system with active targeting cooperative assembly induced retention (AIR) effect. Compared with active targeting mechanism dependent on binding constant K_d , BIVA effect showed an amplified mechanism based on primary binding constant K_d and secondary assembly rate constant K_a (Fig. 5a). To further confirm our hypothesis, the molecule **M1** and **M2** was equally labelled by FITC fluorescence probe for cell imaging (Fig. 5b). To simulate the dynamic physiological condition, the cell culture medium was replaced every 15 min. After 1 h incubation with **M1** and **M2** at the same molecule molar concentration, there were significant differences between the two molecules (Fig. 5c). The **M1** with BIVA effect had higher fluorescence retention rate on the cell membrane, while the **M2** with active targeting mechanism significantly reduced the fluorescence signal during the dynamic incubation. The huge different can be explained by the fact that the secondary assembly rate broke the balance between the targeted ligand and receptor, and thus tended to a stable assembly interaction. The retention efficiency depended on the assembly rate constant K_a . Meanwhile, the rapid dynamic assembly of BIVA probe *in situ* around the cell membrane, contributed to the efficient formation and retention of nanofibers on the cell profile. When delayed the incubation time up to 2 h, some components could be endocytosed into the cells, but most of them were found on the membranes (Supplementary Fig. S15). As shown in Fig. 5d, most molecules of **M1** were assembled and located on the cell membrane within 1 h of incubation. Then, the isolated cells were collected and lysed, the extracted cell membrane fragments were stained with ThT dye. Not surprisingly, the nanofibers on the membrane were all stained by ThT, and the correlation coefficient between ThT and FITC fluorescence was high up to 0.83 (Fig. 5e).

In order to further understand the contribution of the active targeting and AIR effect during locating of the cells. The cell transwell experiment were used to quantitatively evaluate interference of the cell migration

based on different mechanism (Fig. 5f). As expected, untreated cells were easy to migrate to the lower chamber, while the cells treated with active targeting molecule **M2** and assembled molecule **M3**, the migration of cell were reduced. Under the same molar concentration, the **M1** treatment group had most inference on cell migration (Fig. 5g). According to the quantitative statistical calculation of the number of cells (Supplementary Fig. S16), the results in Fig. 5h clearly verified that BIVA effect indeed had a high trapping and localization efficiency around cells. Although the targeting group of **M2** and BIVA group of **M1** had significant interaction with cells, there was no obvious cytotoxicity at high concentration of 300 μ M (Supplementary Fig. S17).

Metabolic difference and optimized biodistribution enhanced imaging. According to the time-dependent *in vivo* NIR images, there were significant differences in the fluorescence distribution among ICG, **M2** and **M1** mice (Fig. 6a). The representative small molecule probe was ICG, which showed rapid distribution and elimination all over the mice body with no obviously specific targeting effect on tumor tissue. The results of near infrared (NIR) imaging showed that ICG completed its metabolic clearance within 8 h. Moreover, the **M2** probe with active targeting capability was distributed and accumulated in the tumor area within 0.1 h-24 h. The metabolized rate from tumor and other tissues seemed no obvious difference. However, the **M1** probe based on BIVA effect optimized the biodistribution, which accumulated more signal in the tumor area and enhanced retention in tumor long lasted up to 96 h. Meantime, the non-tumor tissues showed lower signal distribution resulting a short elimination time. Based on NIR imaging, the **M1** with higher imaging contrast enable to have a stable detection window within 8 h-96 h attributing to the enhanced targeting and metabolic difference of the BIVA probe. Meanwhile, the photoacoustic imaging after *i.v.* injection of **M1** and **M2** for 12 h clearly show the big difference on the tumor signal and the surround tissues, the **M1** had more accumulation in tumor than that of **M2** (Supplementary Fig. S18).

Otherwise, the molecules of **M1** and **M2** with a mPEG tail, both had long-time circulation half-life ($t_{1/2}$), which were 110 ± 3 min and 102 ± 4 min, respectively (Fig. 6b). The blood circulation half-life ($t_{1/2}$) of ICG was 2.5 ± 0.5 min. The short $t_{1/2}$ was related to the rapid distribution and elimination behavior *in vivo*. In order to understand the contribution of these elements to effective availability of imaging probe. The significant parameter of pharmacokinetic: area under the curve (AUC) in tumor tissue were obtained according to the quantitative calculation from fluorescence signal. After quantitative calculation of the concentration of probe in tumor area, the time-dependent curve of **M1** and **M2** were carried out (Fig. 6c). The area under the curve ranges from 0 h to 120 h (AUC 0-120 h) of **M1** was 3.6 times more than that of **M2**, which mean that with a single dose administration, the average fluorescence intensity distribution per unit area of **M1** in tumor tissue was 3.6-fold higher than that of **M2**. The time to peak of **M1** was 4 hours later than **M2**, about at 12 h. The highest signal on tumor of **M1** was 1.8 times higher than **M2**. In addition, the signal elimination of **M1** from tumor was quite slow, only 27.6% was reduced between 12 h and 120 h, while the fluorescence signal of **M2** was disappears completely in the same time interval. Finally, we obtained a stable intraoperative navigation window between 8 h and 96 h for our BIVA probe (**M1**). As the conclusion, the long-term blood circulation and the dynamic enzyme tailoring both helped the continuous accumulation in tumor area. The *in-situ* assembly in tumor tissues slowed down the dynamic

elimination and prolong the elimination time, which contributed to maintain the imaging signal during surgery operation. The FAP- α specific tailoring and assembling of **M1** differed the tumor from the other tissues, which offered better contrast and biodistribution. To evaluate the imaging property of BIVA probe, the orthotopic pancreatic tumor mice model was built. After intravenous injected **M1** and **M2** molecules with a dose of 16 mg/kg for 12 h, the mice were sacrificed. When dissected the spleen, the high contrast signal was clearly observed on the orthotopic tumor area (Fig.7a). Then, all the important organs were dissected for *ex vivo* imaging. The significant difference between **M1** and **M2** on the tissue biodistribution. For BIVA probe **M1**, the distribution on tumor had obviously selectivity, and the molecules had part retention in the metabolic organs (e.g. liver and kidney). Whereas, the **M2** exhibited no significant difference in the biodistribution of lung, kidney and tumor, but most of the molecules were stuck in liver. The huge difference between the two molecules can be explained by the high specific recognition of FAP- α to **M1**, which was conducive to efficient molecular tailoring and assembly in tumor, while the **M2** was non-specific cleavage and accumulation in liver during metabolism. The quantitative analysis results also confirmed the conclusion (Fig.7b). The signal accumulation of FAP- α specific BIVA probe **M1** was twice as much as that of **M2**. Under the same blood circulation time, organ selectivity depended on the specificity of substrate to target enzyme. Its accumulation amount relied on the cleavage rate of enzyme and aggregation efficiency of molecular residues. The primary nucleation of assembly can induce long lasting growth of the fibril in tumor, reduce the metabolic rate, and achieve the retention and accumulation of tumor.

Upon the individual difference, we validated 6 mice under surgery to induce orthotopic tumor in pancreatic head. All the positive results were obtained including the small sized tumor around 2 mm in the diameter (Fig.7c). The *ex vivo* dissection in Fig.7d provided us a fantastic imaging contrast on tumor and the around spleen tissue, which visualized identified the small tumor (~ 2 mm). The statistical results of fluorescence signal on tumor were over 9 folds higher than the surround spleen tissue (Fig.7e). The whole tumor histologic section in Fig.7f and Supplementary Fig. S19 stained by Congo Red full viewed the fibril distribution inside tumor. As known the FAP- α was a membrane located protein, overexpressed on tumor associate fibroblast cell and pancreatic cell surface. The FAP- α specific BIVA probe **M1** were well depicted the tumor margin and interstitial space, which concentrated the signal in tumor for better bioimaging, but the **M2** has no obvious Congo Red, which mean there was no assembly inside tumor.

Acute toxicity evaluation to organs. The acute toxicity evaluation of **M1** to mice were verified by blood biochemistry, hemograms and histological analysis. The representative biomarkers of liver function included alanine aminotransferase (ALT), alkaline phosphatase (ALP), aspartate aminotransferase (AST), total protein (TP) and albumin concentration (ALB). Compared to the healthy group (PBS), there had no obvious hepatic toxicity after i.v. injection of 16 mg/kg of **M1** for 24 h (Fig. 8a). In addition, the hematological assessment results including creatinine (CREA), white blood cells (WBC), red blood cells (RBC), hematocrit (HCT), mean corpuscular volume (WCV), mean corpuscular hemoglobin concentration (MCH), mean corpuscular hemoglobin concentration (MCHC), red cell volume distribution width-coefficient of variation (RDW-CV), platelet (PLT) and mean platelet volume (MPV) were carried out (Fig. 8b). All the above indicators in PBS group and **M1** group appeared normal, which was basically

consistent with the normal range reported in the literature. Then the mice from PBS group and **M1** group were sacrificed for the further histological section analysis of the significant organs. After Hematoxylin and Eosin (H&E) staining, the slices of heart, liver, spleen, lung, kidney and pancreas were compared and evaluated (Fig. 8c). There was no noticeable organ damage and tissue injury of the two groups. All the evidences revealed that under the imaging dose, the BIVA probe had no acute toxicity performance.

Discussion

Although the optical probes had a great potential in the further clinical trials, the druggability still a big issue. As a great improvement, the targeting ligand covalent coupling such as antibody, peptide and etc, significantly increased the targeting property of the probes. However, the optical probes based on active targeting mechanism were always in a narrow imaging window, which cannot meet the need of stable imaging for intraoperative navigation. Thus, we proposed a bioactivated in vivo assembly (BIVA) nanotechnology to fabricate NIR probe, which offered a new targeting mechanism based on synergy of active targeting and AIR effect. The modular designed BIVA probe were specific to pancreatic tumor overexpressed FAP- α , resulting a sensitive transformation from monomers to assemblies *in vitro* and *in vivo*, resulting a high contrast (signal-to-background ratio SBR > 9 folds) imaging window from 8 h to 96 h. Meantime, the mPEG tail provided a long-time blood circulation half-life ($t_{1/2}$) up to 110 min. The assembling triggered by membrane protein FAP- α induced a specific pancreatic tumor cells accumulation around cells. The site-specific assembly contributed to great difference of metabolized time between tumor cells and surround healthy cells, further optimizing the organ distribution. All the efforts realized a highly sensitive small (< 2 mm) orthotopic pancreatic tumor imaging in vivo. We believed that the BIVA nanotechnology would upgrade the imaging probe into clinical drug. The dynamic assembled property and assembled conformation modulation would be optimized according to the surgical imaging needs. Such a delivery system can further be expanded to carry different fluorescent molecules, the resulted BIVA probes will benefit future precision medicine.

Methods

Molecule synthesis and characterization: The peptides were synthesized according to the standard solid phase synthesis method.^[28] The loading value of Wang resin was 0.349 mmol/g. The deprotective agent was a mixture of anhydrous DMF and piperidine with a volume ratio of 4/1. The coupling agent was composed of 5% NMM and 95% anhydrous DMF (V / V). The cleavage agent was a mixture of 92.5% TFA, 2.5% TIPS, 2.5% 1,2-ethanedithiol, 2.5% H₂O (V / V / V / V) solution. mPEG₂₀₀₀-NHS was linked to the N terminal of peptide similar with other amino acid but the reaction time lasted up to 24 h. The IR₇₈₃ (1.1 mol equivalent) was coupled onto peptide (cleaved from the resin) after reacting in Tris buffer at pH = 8.5 for 12 h, washed the unreacted dye in ice bath with DCM, and dialyzed on MWCO 2000 Da dialysis membrane for 24 h. Finally, all the molecules were characterized by Matrix-assisted laser desorption ionization time-of-flight mass spectrometry (MALDI-TOF-MS, Matrix: saturated DHB in TA30) and high-performance liquid chromatography (HPLC, a C18 column and a linear gradient of acetonitrile/water with 0.1% TFA respectively from 10%/90% to 50%/50% and a flow speed of 1 mL/min at 25°C).

Molecular dynamics (MD) simulation: The GROMACS software package (version 5.1.4) was used to perform energy minimization and molecular dynamics simulations using the AMBER99SB-ILDN force field. The topology and force field parameters files for the PEG were generated with Acypye Antechamber. All the structures were solvated in a box of TIP3P water model, and then ionized and neutralized with Na⁺ and Cl⁻ ions as 0.15 mol/L. The periodic boundary conditions (PBC) were set for all directions. The NPT ensemble was applied. After energy minimization, each structure underwent NVT equilibration and NPT production. The Nose-Hoover thermostat^[29] was used to maintain the temperature of system as 300K. The pressure was maintained as 1 atm by coupling the semi-isotropic (X+Y, Z) directions of the system using the Parrinello–Rahman algorithm.^[30] The van der Waals (vdWs) interactions were computed with a cutoff distance as 12 Å, while long-range electrostatic interactions were handled with the particle mesh Ewald (PME) method.^[31] The water molecules were constrained by the SETTLE algorithm,^[32] and the hydrogen bonds were constrained to their equilibrium values employing the LINCS algorithm.^[33] The timestep was 2 ps in production runs, and the coordinates were saved every 100 ps. Totally time of each system was 200 ns. The VMD software was used to observe and draw the image of all systems.

Circular dichroism (CD) spectroscopy: The secondary structures of **M1**, **M3** and **R-M1** were verified by CD spectrum (JASCO Corporation, JC-1500) at room temperature with a cell path length of 1 cm. **M1**, **M2** and **R-M1** were diluted to 100 µM with deionized water at 25 °C and allowed to stand for 12 h for complete assembly. Detail parameter setting were CD scale:200 mdeg/1.0D, measure range: 260~190 nm, scanning speed: 500 nm/min, bandwidth: 1.00 nm, and data pitch: 0.5 nm. All spectra were the average of three measurements.

Fourier transform infrared spectroscopy (FTIR): FTIR was used to analyze the secondary structures and intermolecular interactions of **M1**, **M3** and **R-M1**. **M1**, **M3** and **R-M1** were dispersed in distilled water to 100 µM, and the samples were obtained by standing for 12 h. The liquid sample was freeze-dried. Spectrum range was between 4000-450 cm⁻¹. All results were averaged among 16 measurements. ATR was used to collect the spectrum.

Transmission electron microscopy (TEM): TEM was used to characterize the morphology of the assemblies of **R-M1** and **M1** after enzyme cleavage. The instrument used was TECNAI G2 20 s-twin electron microscope. The sample (20 µL, 100 µM, made of deionized water) after standing for 12 h was dropped onto the copper mesh. After standing for 10 min, the upper liquid was removed and the copper mesh was dyed with 2% uranyl acetate for 1 min. Finally, the surface of the copper mesh was washed with distilled water. The copper mesh was placed overnight at room temperature and then observed.

Nanofiber dynamic growth: ThT solution (1.75 mM) was used to detect the amyloid fibers formed by **R-M1** with emission spectrum shift from 440 nm to 490 nm.

Cytotoxicity assay: The cytotoxicity of **M1** and **M2** was evaluated using CCK-8 assay in MiaPaCa -2 cells. Cells were seeded into 96-well plates at a density of 5 × 10⁴ cells per well and placed in an incubator for 14 h. Subsequently, the sample was diluted into a series of different concentrations (60, 80, 100, 150, 200,

250 and 300 μM) to incubate with cells for 24h. After that, 10 μL of CCK-8 solution was added to each well and incubated for 2 h. The absorbance of blank wells (A_b), sample wells (A_s) and control wells (A_c) were measured with a microplate reader at a test wavelength of 450 nm and a reference wavelength of 690 nm. The cell viability rate (%) is equal to $(A_s - A_b) / (A_c - A_b) \times 100\%$. All experiments were repeated in triplicate.

Cellular imaging experiment: MiaPaCa-2 cells were digested with trypsin, counted with cell counting plate, diluted to 1×10^4 with DMEM medium, and 1 mL to 1 cm diameter confocal microscope dish was taken. The cells were incubated in 37% CO_2 atmosphere for 24 hours. The medium containing **M1** and **M2** (50 μM) was replaced and incubated with the cells for 2 hours. The cells were washed with PBS for 3 times. CLSM (ultraview VOX) was used to image cells under 40 \times objective.

In Vivo and ex vivo fluorescence imaging: All the animal experiments were performed in accordance with the Guide for the Care and Use of Laboratory Animals and approved by the Committee for Animal Research of the National Center for Nanoscience and Technology. The MiaPaCa-2 tumor-bearing mice were intravenously injected with **ICG**, **M1** and **M2** (16 mg/kg), respectively for *in vivo* fluorescence imaging with *in vivo* spectrum imaging system. Finally, mice were sacrificed to collect the major organs and tumors for *ex vivo* fluorescence imaging.

In Vivo Photoacoustic imaging: The MiaPaCa-2 tumor-bearing mice were constructed for *in vivo* photoacoustic imaging of **M1**. After intravenously injected with **M1** (16 mg/kg) through tail vein, the PA images of mice were acquired with MOST (mode: MOST 128) at 12 h post injection.

Establishment of the orthotopic pancreatic cancer xenograft model: Female BALB/c nude mice (6-8 weeks, 16-18 g) were intraperitoneally anesthetized with Pentobarbital sodium (40 mg/kg body weight) and placed in a lateral position (right side down). After the pancreas was exposed under sterile conditions, MiaPaCa-2 cells resuspended in Matrigel were injected into the parenchyma of pancreas of mice. Subsequently, the body wall and skin incision were successively closed after the pancreas was returned into the peritoneal space. After confirming the tumor growth in pancreas, the tumor specific recognition of **M1** and **M2** were investigated with IVIS.

Tumor slices and staining: Tumors were harvest and collected in 4 % paraformaldehyde solution after treated with **M1** at a dose of 16 mg/kg for 12 h. The H&E and Congo red staining procedure was performed by Google biotechnology (Wuhan) co. LTD.

Toxicology evaluation: The female Balb/c nude mice (6-8 weeks, $n = 3$) were sacrificed for blood and major organs collection after treated with **M1** at a dose of 16 mg/kg on the 24 h. The histology evaluation of major organs was performed by Google biotechnology (Wuhan) co. LTD. The blood biochemistry and haematology analyses were carried out by Vital River Laboratory Animal Technology Co. Ltd.

Statistical methods: Data are reported as mean \pm standard deviation. Statistical analysis of the data was performed with one-way ANOVA followed by post hoc Tukey's test. Statistical significance was defined as

*p < 0.05, **p < 0.01 and ***p < 0.001.

Declarations

Acknowledgments

This work was supported by the National Key R&D Program of China (2018YFE0205400), National Natural Science Foundation of China (51873045), CAS Interdisciplinary Innovation Team and Youth Innovation Promotion (2017053).

Author contributions

L.-L. Li, H. Ren and X.-X. Zhao conceived and designed the project. H. Ren and X.-X. Zhao carried out the synthesis and characterization of the BIVA probes. H. Yao and L. Zhao contributed the molecular dynamics (MD) simulation calculations parts. H. Ren and D. Hou performed the fluorescence imaging studies both in vitro and in vivo. L.-L. Li, H. Ren and D. Hou co-wrote the manuscript. All authors interpreted data, provided critical insights, and edited the manuscript.

Additional information

Supporting Information is available in the online version of the paper. Reprints and permissions information is available online at www.nature.com/reprints. Correspondence and requests for materials should be addressed to L.-L. L.

Competing financial interests

The authors declare no competing financial interests.

References

1. Mueller, S.,Engleitner, T.,Maresch, R.,Zukowska, M.,Lange, S.,Kaltenbacher, T.,Konukiewitz, B.,Öllinger, R.,Zwiebel, M.,Strong, A.,Yen, H. Y.,Banerjee, R.,Louzada, S.,Fu, B.,Seidler, B.,Götzfried, J.,Schuck, K.,Hassan, Z.,Arbeiter, A.,Schönhuber, N.,Klein, S.,Veltkamp, C.,Friedrich, M.,Rad, L.,Barenboim, M.,Ziegenhain, C.,Hess, J.,Dovey, O. M.,Eser, S.,Parekh, S.,Constantino-Casas, F.,de la Rosa, J.,Sierra, M. I.,Fraga, M.,Mayerle, J.,Klöppel, G.,Cadiñanos, J.,Liu, P.,Vassiliou, G.,Weichert, W.,Steiger, K.,Enard, W.,Schmid, R. M.,Yang, F.,Unger, K.,Schneider, G.,Varela, I.,Bradley, A.,Saur, D.,Rad, R., Evolutionary routes and KRAS dosage define pancreatic cancer phenotypes. *Nature*. **554**, 62-68(2018).
2. Siegel, R. L.,Miller, K. D.,Jemal, A., Cancer statistics, 2020. *CA Cancer J Clin*. **70**, 7-30(2020).
3. Mizrahi, J. D.,Surana, R.,Valle, J. W.,Shroff, R. T., Pancreatic cancer. *Lancet*. **395**, 2008-2020(2020).
4. Pereira, S. P.,Oldfield, L.,Ney, A.,Hart, P. A.,Keane, M. G.,Pandol, S. J.,Li, D.,Greenhalf, W.,Jeon, C. Y.,Koay, E. J.,Almario, C. V.,Halloran, C.,Lennon, A. M.,Costello, E., Early detection of pancreatic cancer. *Lancet Gastroenterol Hepatol*. **5**, 698-710(2020).

5. Triponez, F., Goudet, P., Dosseh, D., Cougard, P., Bauters, C., Murat, A., Cadiot, G., Niccoli-Sire, P., Calender, A., Proye, C. A., Is surgery beneficial for MEN1 patients with small (< or = 2 cm), nonfunctioning pancreaticoduodenal endocrine tumor? An analysis of 65 patients from the GTE. *World J Surg.* **30**, 654-62; discussion 663-4(2006).
6. Kindler, H. L., A Glimmer of Hope for Pancreatic Cancer. *N Engl J Med.* **379**, 2463-2464(2018).
7. Pannala, R., Basu, A., Petersen, G. M., Chari, S. T., New-onset diabetes: a potential clue to the early diagnosis of pancreatic cancer. *The Lancet. Oncology.* **10**, 88-95(2009).
8. Bouziotis, P., Molecular imaging and therapy in nuclear medicine. *Curr Top Med Chem.* **12**, 2641(2012).
9. Wang, P., Fan, Y., Lu, L., Liu, L., Fan, L., Zhao, M., Xie, Y., Xu, C., Zhang, F., NIR-II Nanoprobes In-Vivo Assembly to Improve Image-Guided Surgery for Metastatic Ovarian Cancer. *Nat Commun.* **9**, 2898(2018).
10. Glasenapp, A., Hess, A., Thackeray, J. T., Molecular imaging in nuclear cardiology: Pathways to individual precision medicine. *J Nucl Cardiol.* **27**, 2195-2201(2020).
11. Vahrmeijer, A. L., Hutteman, M., van der Vorst, J. R., van de Velde, C. J. H., Frangioni, J. V., Image-Guided Cancer Surgery Using Near-Infrared Fluorescence. *Nature Reviews Clinical Oncology.* **10**, 507-518(2013).
12. Zhang, C., Liu, T., Luo, P., Gao, L., Liao, X., Ma, L., Jiang, Z., Liu, D., Yang, Z., Jiang, Q., Wang, Y., Tan, X., Luo, S., Wang, Y., Shi, C., Near-infrared oxidative phosphorylation inhibitor integrates acute myeloid leukemia-targeted imaging and therapy. *Sci Adv.* **7**, eabb6104(2021).
13. Chiu, C. C., Sentinel Lymph Node Biopsy in Breast Cancer Guided by Indocyanine Green Fluorescence. *Br J Surg.* **97**, 455-455(2010).
14. Huang, J., Pu, K., Activatable Molecular Probes for Second Near-Infrared Fluorescence, Chemiluminescence, and Photoacoustic Imaging. *Angew Chem Int Ed.* **59**, 11717-11731(2020).
15. Zhen, X., Jiang, X., Polymer-based activatable optical probes for tumor fluorescence and photoacoustic imaging. *Wiley Interdiscip Rev Nanomed Nanobiotechnol.* **12**, e1593(2020).
16. Wang, S., Zhang, L., Zhao, J., He, M., Huang, Y., Zhao, S., A tumor microenvironment-induced absorption red-shifted polymer nanoparticle for simultaneously activated photoacoustic imaging and photothermal therapy. *Sci Adv.* **7**, eabe3588(2021).
17. Longmire, M., Choyke, P. L., Kobayashi, H., Clearance Properties of Nano-Sized Particles and Molecules as Imaging Agents: Considerations and Caveats. *Nanomed.* **3**, 703-717(2008).
18. Huang, J., Li, J., Lyu, Y., Miao, Q., Pu, K., Molecular optical imaging probes for early diagnosis of drug-induced acute kidney injury. *Nat Mater.* **18**, 1133-1143(2019).
19. Cai, Y., Shen, H., Zhan, J., Lin, M., Dai, L., Ren, C., Shi, Y., Liu, J., Gao, J., Yang, Z., Supramolecular "Trojan Horse" for Nuclear Delivery of Dual Anticancer Drugs. *J Am Chem Soc.* **139**, 2876-2879(2017).
20. Zhao, X.-X., Li, L.-L., Zhao, Y., An, H.-W., Cai, Q., Lang, J.-Y., Han, X.-X., Peng, B., Fei, Y., Liu, H., Qin, H., Nie, G., Wang, H., *In Situ* Self-Assembled Nanofibers Precisely Target Cancer-Associated Fibroblasts for Improved Tumor Imaging. *Angew Chem Int Ed.* **58**, 15287-15294(2019).

21. An, H.-W., Li, L.-L., Wang, Y., Wang, Z., Hou, D., Lin, Y.-X., Qiao, S.-L., Wang, M.-D., Yang, C., Cong, Y., Ma, Y., Zhao, X.-X., Cai, Q., Chen, W.-T., Lu, C.-Q., Xu, W., Wang, H., Zhao, Y., A Tumour-Selective Cascade Activatable Self-Detained System for Drug Delivery and Cancer Imaging. *Nat Commun.* **10**, 4861(2019).
22. Hata, H., Nishiyama, M., Kitao, A., Molecular dynamics simulation of proteins under high pressure: Structure, function and thermodynamics. *Biochim Biophys Acta Gen Subj.* **1864**, 129395(2020).
23. Liang, Y., Pingali, S. V., Jogalekar, A. S., Snyder, J. P., Thiyagarajan, P., Lynn, D. G., Cross-strand pairing and amyloid assembly. *Biochemistry.* **47**, 10018-26(2008).
24. Pieszka, M., Han, S., Volkmann, C., Graf, R., Lieberwirth, I., Landfester, K., Ng, D. Y. W., Weil, T., Controlled Supramolecular Assembly Inside Living Cells by Sequential Multistaged Chemical Reactions. *J Am Chem Soc.* **142**, 15780-15789(2020).
25. Han, S., Kim, D., Han, S. H., Kim, N. H., Kim, S. H., Lim, Y. B., Structural and conformational dynamics of self-assembling bioactive β -sheet peptide nanostructures decorated with multivalent RNA-binding peptides. *J Am Chem Soc.* **134**, 16047-53(2012).
26. Kriebisch, B. A. K., Jussupow, A., Bergmann, A. M., Kohler, F., Dietz, H., Kaila, V. R. I., Boekhoven, J., Reciprocal Coupling in Chemically Fueled Assembly: A Reaction Cycle Regulates Self-Assembly and Vice Versa. *J Am Chem Soc.* **142**, 20837-20844(2020).
27. Schved, F., Lindner, P., Juven, B. J., Interaction of the bacteriocin pediocin SJ-1 with the cytoplasmic membrane of sensitive bacterial cells as detected by ANS fluorescence. *J Appl Bacteriol.* **76**, 30-35(1994).
28. An, H.-W., Hou, D., Zheng, R., Wang, M.-D., Zeng, X.-Z., Xiao, W.-Y., Yan, T.-D., Wang, J.-Q., Zhao, C.-H., Cheng, L.-M., Zhang, J.-M., Wang, L., Wang, Z.-Q., Wang, H., Xu, W., A Near-Infrared Peptide Probe with Tumor-Specific Excretion-Retarded Effect for Image-Guided Surgery of Renal Cell Carcinoma. *ACS Nano.* **14**, 927-936(2020).
29. Hoover, W. G., Canonical dynamics: Equilibrium phase-space distributions. *Phys Rev A Gen Phys.* **31**, 1695-1697(1985).
30. A, R., Polymorphic Transitions in Single Crystals: a New Molecular Dynamics Method. *J Appl Phys.* **52**, 7182(1981).
31. Darden, T., York, D., Pedersen, L., PARTICLE MESH EWALD - AN N.LOG(N) METHOD FOR EWALD SUMS IN LARGE SYSTEMS. *J Chem Phys.* **98**, 10089-10092(1993).
32. Miyamoto, S., Kollman, P. A., SETTLE - AN ANALYTICAL VERSION OF THE SHAKE AND RATTLE ALGORITHM FOR RIGID WATER MODELS. *J Comput Chem.* **13**, 952-962(1992).
33. Hess, B., Bekker, H., Berendsen, H. J. C., Fraaije, J. G. E. M., LINCS: A linear constraint solver for molecular simulations. *J Comput Chem.* **18**, 1463-1472(1997).

Figures

Bioactivated *In Vivo* Assembly (BIVA) probe

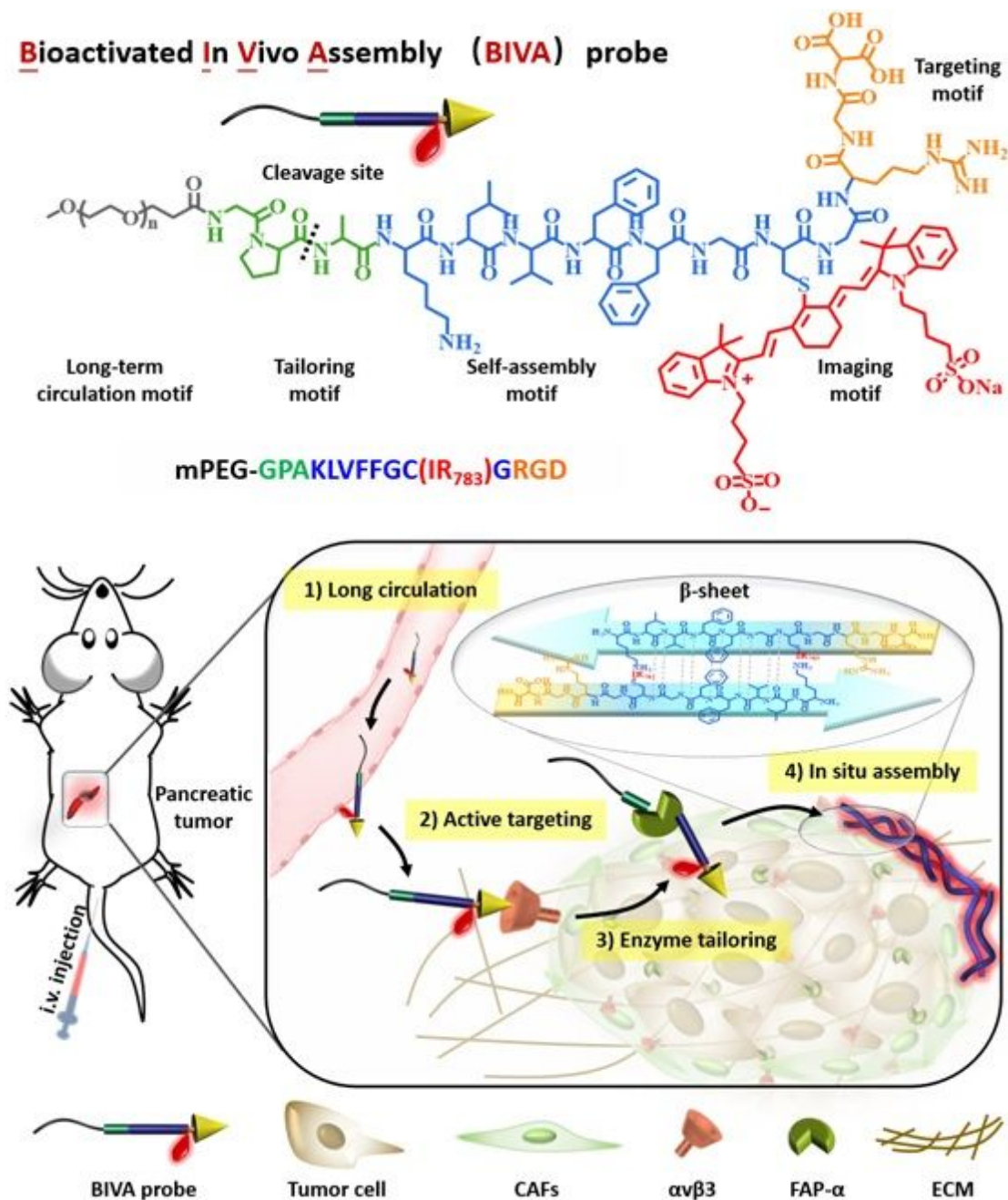


Figure 1

Chemical structure of bioactivated in vivo assembly (BIVA) probe. The long-term circulation property of BIVA probe offered more opportunity for active targeting. Then, the enzyme (FAP- α) on the surface of tumor cell specifically tailored the probe and induced in situ nano-assemblies. The β -sheet assemblies exhibited a site-specific location around the CAFs and a prolonged accumulation for better pancreatic tumor intraoperative navigation.

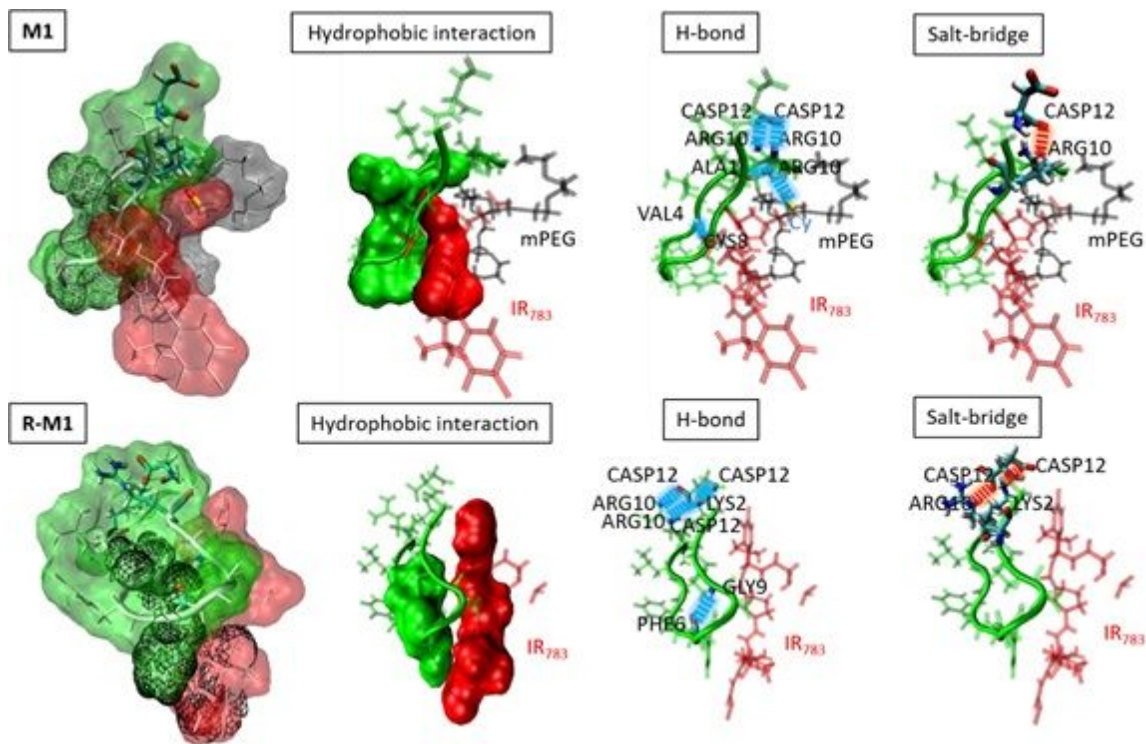


Figure 2

The molecular dynamics (MD) simulation of M1 and R-M1. The molecular interaction details including hydrogen bond (blue dotted-line), salt-bridge (red dotted-line) and hydrophobic interaction. Red part: IR783; Gray part: mPEG2000; Green part: peptide.

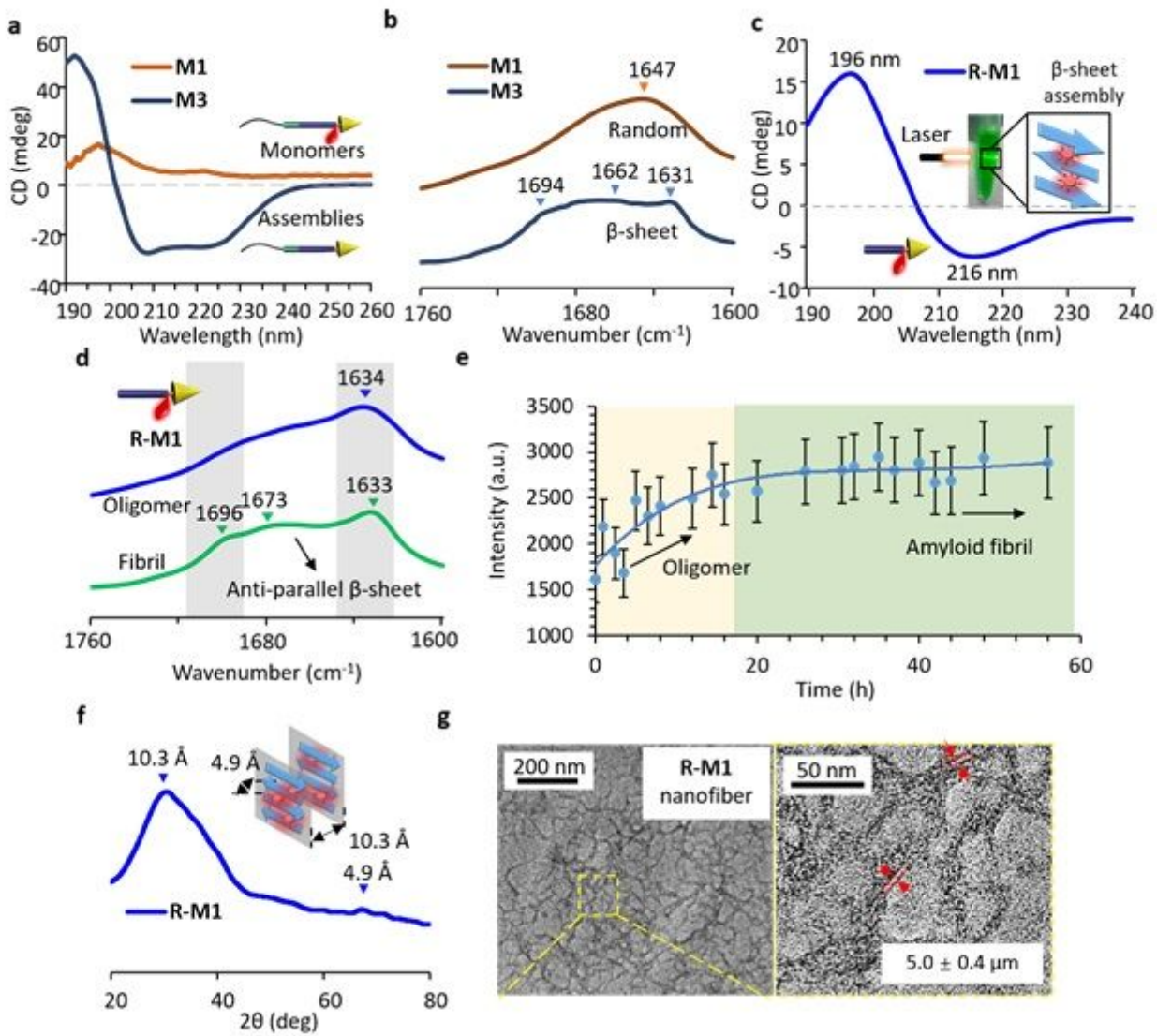


Figure 3

Assembled structure conformations and self-assembly behavior in aqueous solution. a, CD spectra of M1 and M3 in DI water under a concentration of 200 μM. b, the FTIR spectra of M1 and M3. c, The typical β-sheet CD spectra of R-M1 in DI water (insert figure: the Dundal phenomenon) under a concentration of 100 μM. d, the FTIR spectra of dynamic growth of R-M1. e, elongation-nucleation growth procedure with ThT staining. f, the WAXS spectrum and illustration of the R-M1 fibrils. g, the TEM images of nanofibers morphology of R-M1. Data: mean ± standard deviation (n=3).

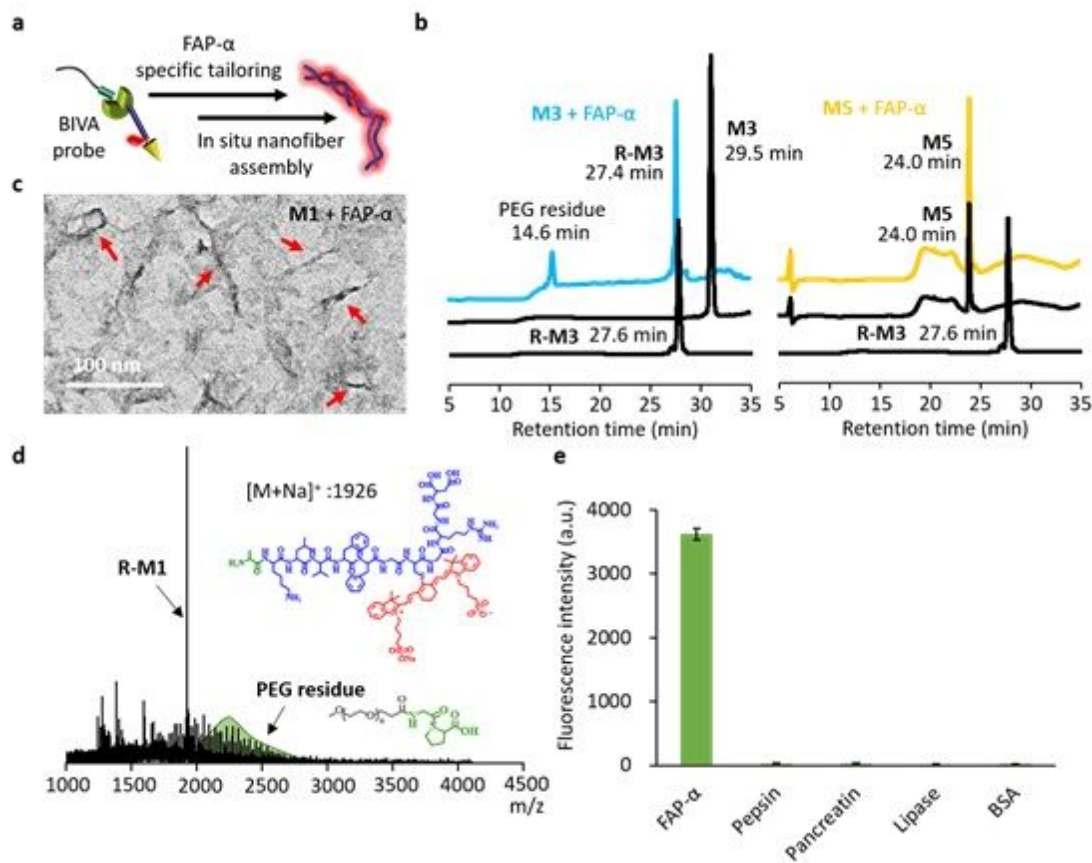


Figure 4

The FAP- α specific molecule tailoring and inducing in situ assembly. a, the illustration the working mechanism of BIVA probe based on FAP- α catalytic hydrolysis. b, HPLC curves of M3 and M5 after incubation with FAP- α in buffer. R-M3, M3 and M5 were synthesized controls. the TEM image c, and the MALDI-TOF d, results of M1 after tailoring by FAP- α in buffer. e, the enzyme specificity of M1 in buffer. Buffer: 50 mM Tris, 1m NaCl, 1 mg/mL, BSA, pH 7.5; Concentration of M1 and M3: 100 μ M; Concentration of FAP- α : 50 mM; Incubation time: 12 h.

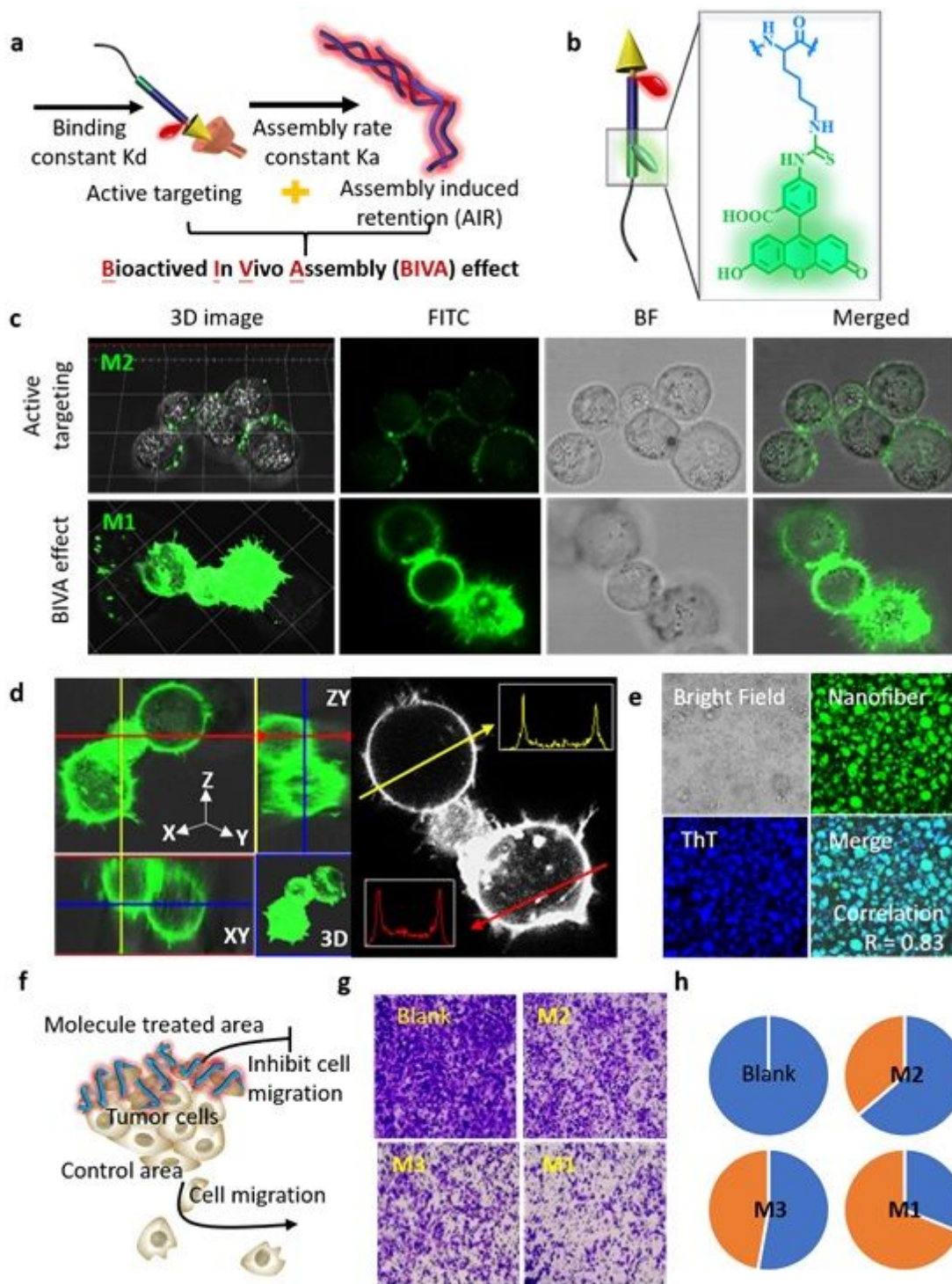


Figure 5

The BIVA effect with enhanced targeting to pancreatic tumor cell for outline location imaging. a, Illustration of BIVA effect: active targeting and assembly induced retention (AIR). b, Chemical structure of FITC labeling. c, 2D and 3D confocal images of M2 with active targeting property and M1 with BIVA effect on Miapaca-2 cells after incubation for 1 h. d, The distribution of M1 on Miapaca-2 cell. e, ThT staining of the lysed cell membrane of Miapaca-2. f, Illustration of migration inhibition after treated by BIVA probe. g, The image of the transferred cells after treatment of PBS (blank), M2, M3 and M1. h, The pie diagram of quantitative statistical calculation of the transferred cell in different groups.

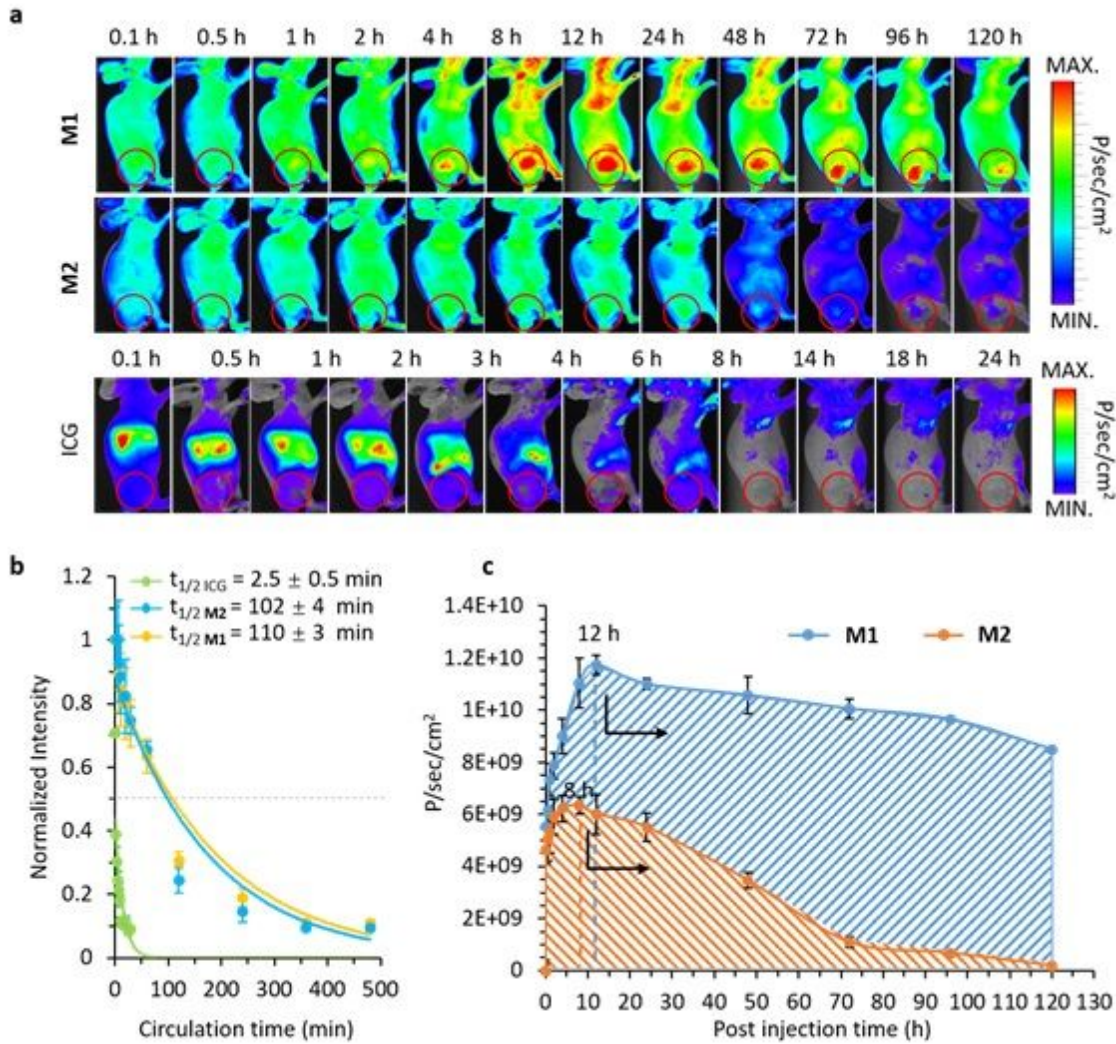


Figure 6

The BIVA effect optimized the metabolism of the probe in vivo. a, The time-dependent NIR fluorescence image of mice bearing Miapaca-2 cells after intravenous administration of ICG, M2 and M1 with a dose of 16 mg/kg. The images acquired at time intervals from 0.1 h to 120 h are managed with the same procedure. b, the blood circulation curve of ICG, M2 and M1 based on exponential curve fitting. The $t_{1/2}$ value was the blood circulation half-life. c, The time-dependent quantitative calculation of the fluorescence in tumor area and the area under the curve (AUC) of ICG, M2 and M1. Data: mean \pm standard deviation (n=3).

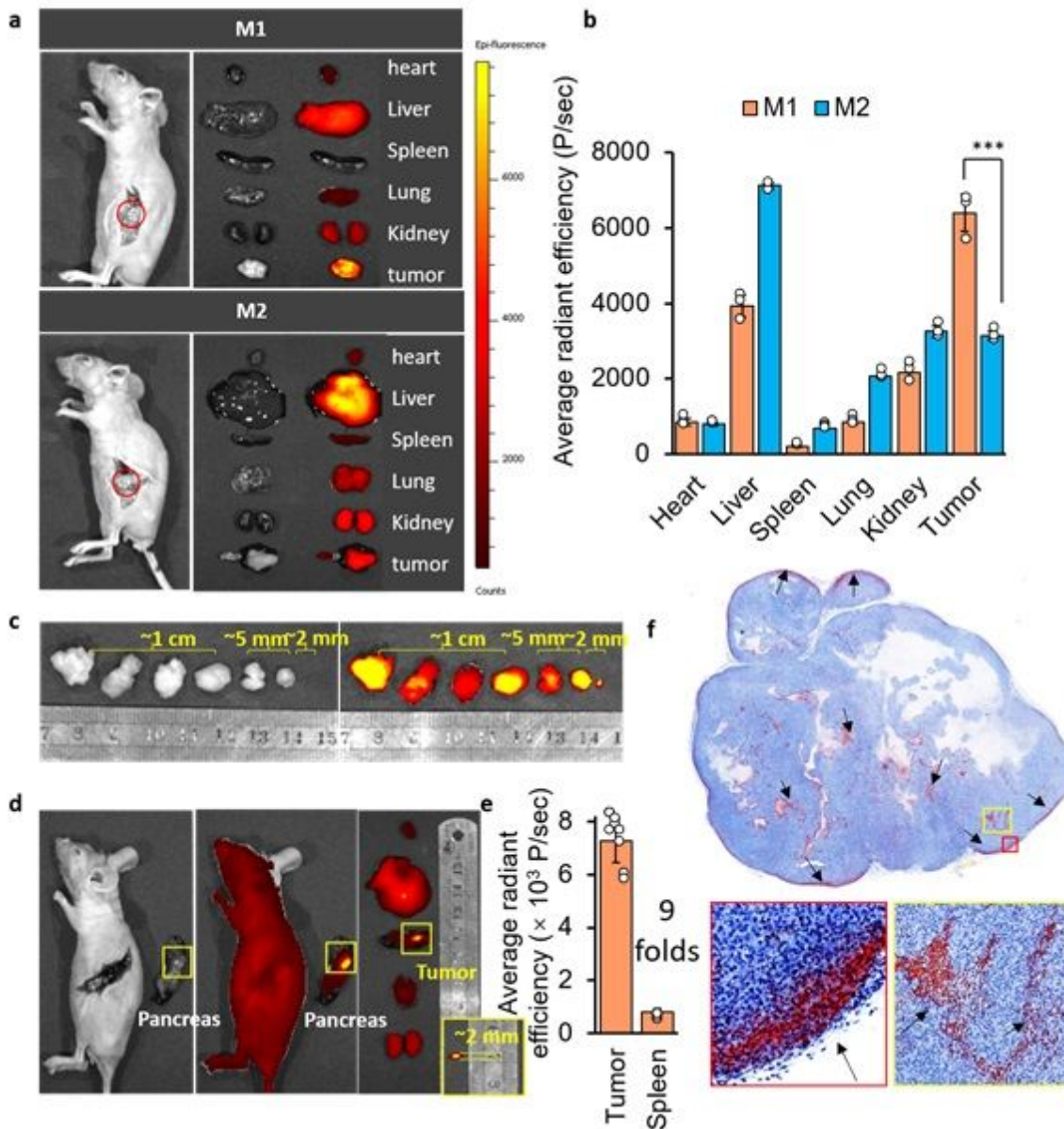


Figure 7

The BIVA probe enhance orthotopic pancreatic tumor imaging in vivo. a, The in vivo NIR images of small orthotopic pancreatic tumor by M1 and M2, and the ex vivo of organ biodistribution including heart, liver, spleen, lung, kidney, and tumor. n=3 b, The quantitative analysis of average fluorescence intensity per organ area. c, The in vivo NIR images of orthotopic pancreatic tumor with individual difference with the same i.v. dose administration for 12 h (n=5). d, The small size (~ 2 mm diameter) orthotopic pancreatic tumor images and its ex vivo signal distribution. e, The quantitative calculation of the signal in tumor area and healthy spleen area (n=8). f, The whole tumor histologic section with congo red (red) stained assembled fibrils. Two enlarged images were respectively corresponded to the red and yellow box. Data: mean \pm standard deviation. Injection dose (i.v. administration): 16 mg/kg. Statistical analysis: one-way ANOVA followed by post hoc Tukey's test, ***p<0.001.

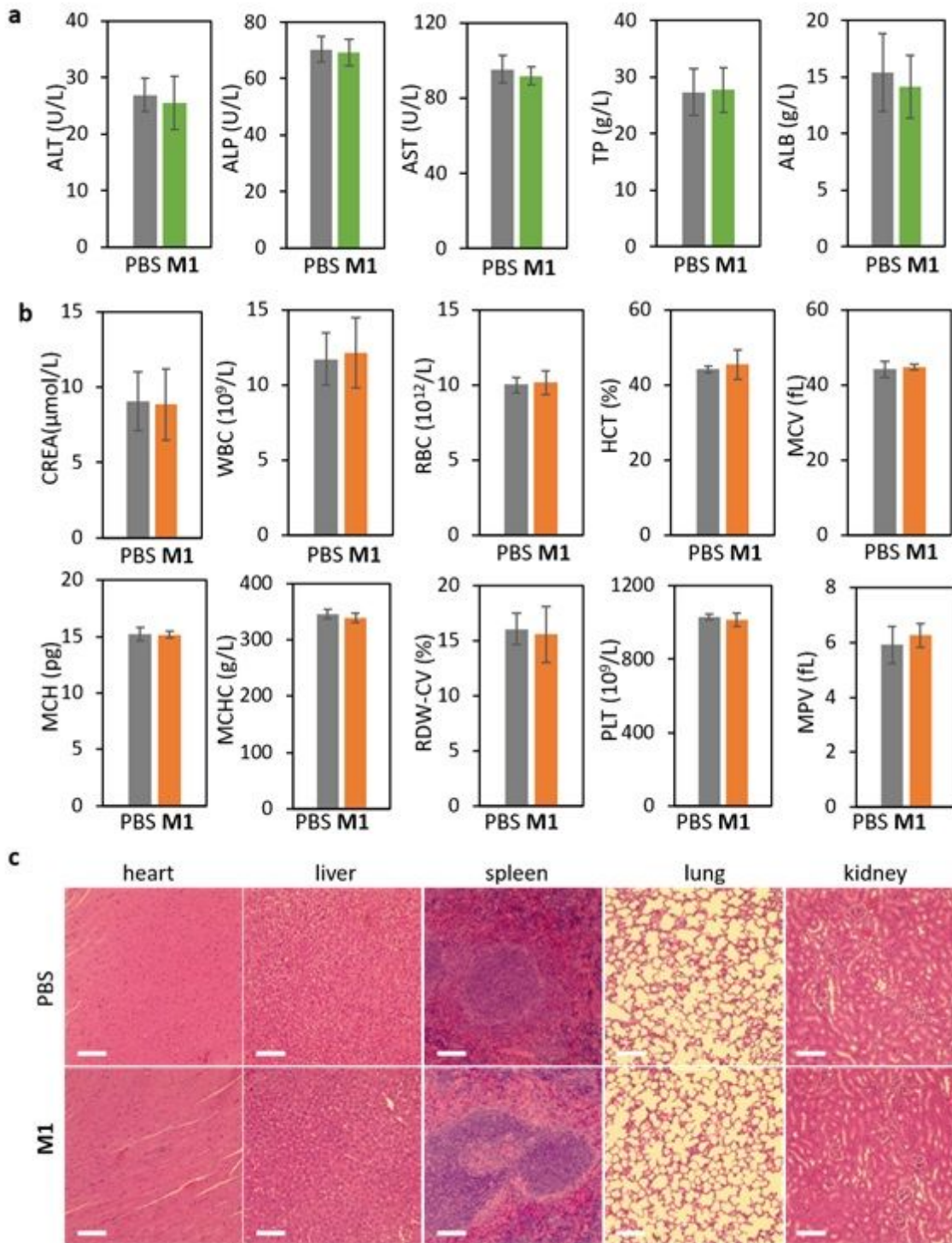


Figure 8

Acute toxicity evaluation. a, Liver function indicators: alanine aminotransferase (ALT), alkaline phosphatase (ALP), aspartate aminotransferase (AST), total protein (TP) and albumin concentration (ALB). b, Blood biochemical indicators: creatinine (CREA), white blood cells (WBC), red blood cells (RBC), hematocrit (HCT), mean corpuscular volume (WCV), mean corpuscular haemoglobin concentration (MCH), mean corpuscular hemoglobin concentration (MCHC), red cell volume distribution width-coefficient of variation (RDW-CV), platelet (PLT) and mean platelet volume (MPV). c, Histologic sections of

different organs: heart, liver, spleen, lung, kidney and pancreas compared with healthy group (PBS).
Staining: H&E; Injection dose of M1. (i.v. administration): 16 mg/kg; Administration time: 24 h.

Supplementary Files

This is a list of supplementary files associated with this preprint. Click to download.

- [reportingsummarywrdfat.pdf](#)
- [SI.docx](#)